Lawrence Berkeley Laboratory
UNIVERSITY OF CALIFORNIA

Materials & Molecular Research Division

A MATHEMATICAL MODEL FOR PREDICTION OF CURRENTS, MAGNETIC FIELDS, MELT VELOCITIES, MELT TOPOGRAPHY AND CURRENT EFFICIENCY IN HALL-HÉROULT CELLS

J.W. Evans, Y. Zundelevich, and D. Sharma
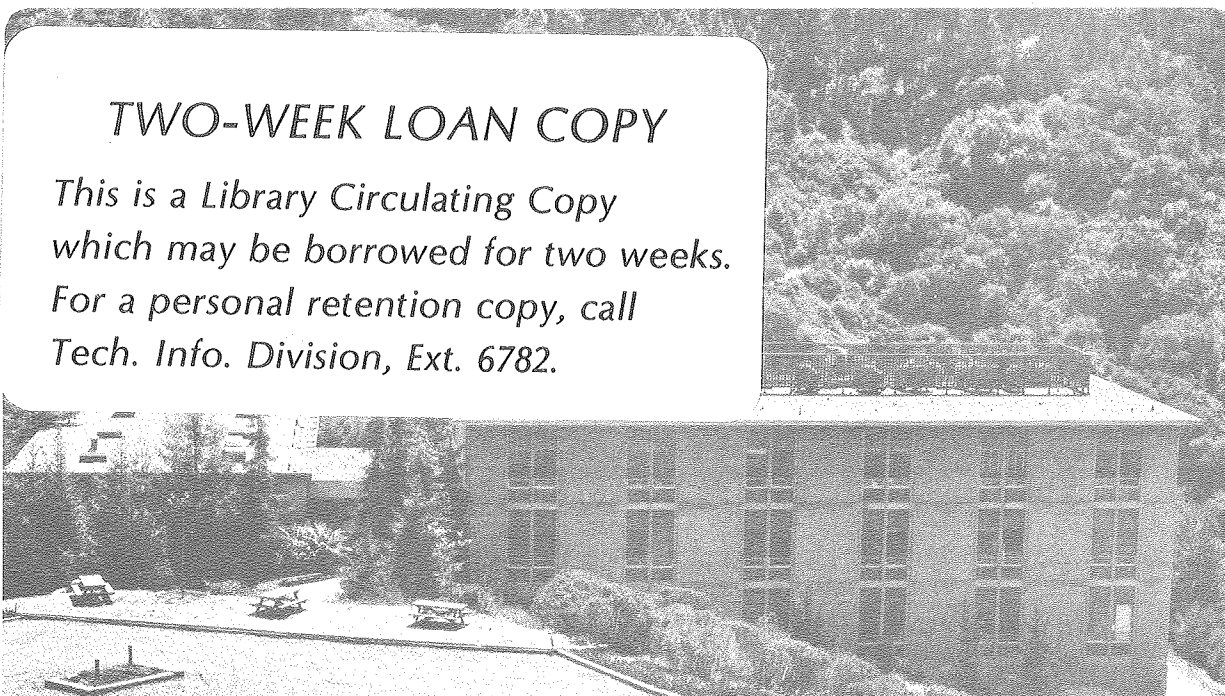
October 1980

TWO-WEEK LOAN COPY

This is a Library Circulating Copy which may be borrowed for two weeks. For a personal retention copy, call Tech. Info. Division, Ext. 6782.

DISCLAIMER

A Mathematical Model for Prediction of

Currents, Magnetic Fields, Melt Velocities,

Melt Topography and Current Efficiency in

Hall-Héroult Cells

J. W. Evans (Principal Investigator, Molecular and Materials
Research Division, Lawrence Berkeley Laboratory and
Professor of Metallurgy, Department of Materials Science and
Mineral Engineering, University of California, Berkeley, CA
94720 - correspondence should be addressed to the latter address)

Y. Zundelevich (Lawrence Berkeley Laboratory)

    and

D. Sharma (Dames and Moore, Denver, Colorado 80215)

ABSTRACT

The magnetic fields, current densities, metal and electrolyte velocities, current efficiencies and topography of the electrolyte-metal interface within the Hall-Héroult cells used to produce aluminum have been predicted from first principles. The computation of current densities was carried out by solving Ohms law enabling the calculation of magnetic field vectors from the Biot-Savart law. The cross product of the current densities and magnetic fields then yielded the electromagnetic stirring forces acting on the molten metal and electrolyte. By employing a turbulence model and the time averaged Navier-Stokes equations, velocities within these two liquids could be calculated. The solution of the fluid flow equations yielded the pressure distribution within both electrolyte and metal, permitting the calculation of the shape of the interface between these two liquids.

INTRODUCTION

Almost all the aluminum manufactured in the U.S. is produced in a Hall-Héroult cell in which aluminum oxide, dissolved in a molten cryolite electrolyte, is electrolytically reduced to metal. Approximately 100 billion kWh per year of electrical energy are consumed in this operation and there is, therefore, considerable incentive for improving the performance of the cell.

Part of a cell is shown in cross section in Fig. 1. The molten cryolite is seen to be floating on a pool of molten aluminum. Dipping into the cryolite is a carbon anode and the surface of the molten metal forms the cathode at which the metal is generated. The anode reaction is the generation of carbon dioxide. Cell performance is adversely affected by electromagnetic stirring forces within the molten cryolite and aluminum. A typical modern cell would have a current of 100-200 kiloamps flowing in a predominantly downward direction from anode to cathode. This current, and currents flowing in adjacent cell components, generate strong magnetic fields, of the order of 100 gauss acting predominantly in the horizontal direction. The interaction of these currents and fields causes a circulation of both cryolite and metal with velocities of the order of 10 cm/sec. Deterioration of the carbon cell lining is promoted by this circulation which also has the effect of reducing the current efficiency of the cell. This reduction in current efficiency arises from the fact that the metallic aluminum generated in the cell has a small solubility in molten cryolite. This dissolved aluminum is transported to the anode region where it is re-oxidized by carbon dioxide bubbles (1). This transport and re-oxidation of product, illustrated in Fig. 1, results in a loss of current efficiency, which in a typical cell is 85-95%. The transport of the dissolved aluminum is

promoted by the turbulence within the cryolite caused by the electromagnetic stirring. This investigation has, as one objective, the prediction of the electromagnetic stirring and current efficiency from first principles and thereby providing a means for developing cell designs or operating procedures with higher current efficiencies. A second objective is the prediction of the topography of the interface between the electrolyte and the aluminum. The electromagnetic forces cause a bowing of this interface such that the interface is typically higher in the center of the cell than at the walls. Reduction of the distance between anodes and the interface results in a reduction of the resistive component of the cell voltage and consequently the energy consumption. Bringing the anodes closer to the metal would be facilitated by a reduction of this bowing of the interface.

The task is fourfold. First the currents and magnetic fields must be calculated as a function of position in the cell, yielding the electromagnetic force distribution. Secondly, the turbulent fluid flow equations must be solved with this force distribution to yield velocities and turbulence levels in the cell. The solution of the fluid flow equations yields the pressure distribution within the electrolyte and metal, from which the topography of the electrolyte-metal interface can be computed. Finally, the rate of transport of aluminum to the anodes and the current efficiency can be calculated, from the turbulence kinetic energy distribution within the electrolyte.

COMPUTATION OF CURRENTS AND MAGNETIC FIELDS

The current distribution within the cell was calculated by the application of Ohm's law:

$$\hat{J} = -\sigma \nabla E \tag{1}$$

Since current is conserved within the cell

$$\nabla \cdot \hat{J} = 0 \qquad (2)$$

and consequently

$$\nabla \cdot \sigma \nabla E = 0 \qquad (3)$$

It should be recognized that σ will be different in different regions of the cell and that equations (1) - (3) are being used to describe both ionic conduction in the molten electrolyte and electronic conduction in the carbon lining, collector bars, metal pools, etc. A discontinuity in potential occurs at the anode/electrolyte interface and at the electrolyte/metal interface due to the electrolytic reactions taking place at these points. The magnitude of these discontinuities (henceforth the electrochemical potential drop) are known (2). The potential, E, in equations (1) and (3) is therefore defined as the potential with respect to the potential of the collector bar end in the carbon lining, metal pool or collector bar. In the cryolite the potential is defined as the potential with respect to the collector bar end, less the potential difference required to drive the electrochemical reaction at the metal-electrolyte interface. In this way the potential E will be continuous throughout the cell.

A rigorous solution of equation (1) would be a three dimensional one with allowance made for a flow of current in the long horizontal dimension (x direction, see Fig. 2) of the cell. In fact, currents in this direction are usually small compared to horizontal current running in the short cell dimension (y direction) and to the (even greater) currents running in a vertical direction (z direction). Consequently a considerable saving in computer time can be realized by solving the equations in two dimensions (z and y). Additional savings in computer time were realized by exploiting the symmetry of the cell,

i.e., the midplane y = constant was assumed to be a surface across which current did not flow. Further boundary conditions employed in the calculation were ones of zero value for E at the ends of the collector bars (by definition) and a value for E equal to the total cell voltage drop less voltage drops for electrochemical reactions at the electrolyte-anode interface. Finally the top surface of the electrolyte and the interface between the carbon cell lining and the refractory (which lies between the carbon and the steel shell) were assumed to be insulating (zero gradient of E normal to the interface). The numerical technique employed in the computations was a finite element procedure of 747 nodes.

The current density distribution having been determined within the cell, the magnetic field strength and direction at any point can be determined by application of the Biot-Savart law in integral form:

$$\hat{H} = \iiint \hat{J} \times \frac{(\hat{r} - \hat{r}')}{|\hat{r} - \hat{r}'|^3} \, dx' dy' dz' \tag{4}$$

where $(\hat{r} - \hat{r}')$ is the radius vector from the point $(\hat{r})$ at which the field strength vector H is to be determined to a point $(\hat{r}')$ at which the current density is J. The integration is over all volume elements in and around the cell. Strictly equation (4) cannot be applied to the calculation of the magnetic field contribution for current carrying elements outside the cell (ring bus, etc.). This is because the inside of the cell is at least partly shielded by the steel shell. This is accounted for by use of an attenuation factor for contributions from the ring bus, as suggested by Robl (3). It should be noted that while the solution of equation (3) was two dimensional, the integration on the right hand side of equation (4) was carried out (numerically) over three dimensions.

The current densities and magnetic fields having been determined at points within the cell, the electromagnetic stirring forces are readily calculated from

$$\hat{F} = \mu \hat{J} \times \hat{H} \tag{5}$$

COMPUTATION OF ELECTROLYTE AND METAL VELOCITIES

In the aluminum cell the electrolyte and metal move under the influence of three forces. These forces are the electromagnetic stirring force (assumed to be dominant in this study), bouyancy forces due to temperature and concentration gradients, and bouyancy due to the presence of gas bubbles in the electrolyte adjacent to the anode. Only the first kind of force is taken into account here. Since the predominant direction of current flow is vertical, the predominant magnetic field direction is a horizontal one and the predominant electromagnetic stirring force is horizontal (perpendicular to the direction of the predominant magnetic field). Consequently the most significant effect of the electromagnetic field is the stirring of the metal and electrolyte in a horizontal direction. In this study it was therefore assumed that vertical velocity components could be neglected, vertical convection of momentum was thereby treated as negligible and it was also assumed that diffusive (viscous) transport of momentum in a vertical direction was negligible.

As a consequence of these assumptions the time averaged Navier Stokes equations become:

$$\rho U \frac{\partial U}{\partial x} + \rho V \frac{\partial U}{\partial y} = -\frac{\partial P}{\partial x} + \frac{\partial}{\partial x}\left(\mu_e \frac{\partial U}{\partial x}\right) + \frac{\partial}{\partial y}\left(\mu_e \frac{\partial U}{\partial y}\right) + \rho F_x \tag{6}$$

$$\rho U \frac{\partial V}{\partial x} + \rho V \frac{\partial V}{\partial y} = -\frac{\partial P}{\partial y} + \frac{\partial}{\partial x}\left(\mu_e \frac{\partial V}{\partial x}\right) + \frac{\partial}{\partial y}\left(\mu_e \frac{\partial V}{\partial y}\right) + \rho F_y \tag{7}$$

These two equations must be solved in conjunction with the equation of continuity:

$$\frac{\partial V}{\partial x} + \frac{\partial U}{\partial y} = 0 \tag{8}$$

The effective viscosity appearing in equations (6) and (7) is the sum of the ordinary (laminar) viscosity and a turbulent viscosity introduced to account for the transport of momentum by Reynolds stresses, i.e.,

$$\mu_e = \mu_1 + \mu_t \tag{9}$$

The turbulent contribution to the viscosity, μ_t, was calculated using the k-ε model for turbulence developed by Spalding, Launder and coworkers (4). In this turbulence model μ_t is given by

$$\mu_t = 0.09 \frac{\rho k^2}{\varepsilon} \tag{10}$$

These two turbulence quantities are obtained from two additional transport equations:

$$U \frac{\partial k}{\partial x} + V \frac{\partial k}{\partial y} = \frac{1}{\rho} \frac{\partial}{\partial x} \left[\frac{\mu_t}{\sigma_k} \frac{\partial k}{\partial x} \right] + \frac{1}{\rho} \frac{\partial}{\partial y} \left[\frac{\mu_t}{\sigma_k} \frac{\partial k}{\partial y} \right]$$

$$+ \frac{\mu_t}{\rho} \left[\left(\frac{\partial U}{\partial y} + \frac{\partial V}{\partial x} \right)^2 + 2 \left(\frac{\partial U}{\partial x} \right)^2 + 2 \left(\frac{\partial V}{\partial y} \right)^2 \right] - \varepsilon \tag{11}$$

$$U \frac{\partial \varepsilon}{\partial x} + V \frac{\partial \varepsilon}{\partial y} = \frac{1}{\rho} \left[\frac{\mu_t}{\sigma_\varepsilon} \frac{\partial \varepsilon}{\partial x} \right] + \frac{1}{\rho} \frac{\partial}{\partial y} \left[\frac{\mu_t}{\sigma_\varepsilon} \frac{\partial \varepsilon}{\partial y} \right]$$

$$+ C_1 \frac{\mu_t}{\rho} \frac{\varepsilon}{k} \left[\left(\frac{\partial U}{\partial y} + \frac{\partial V}{\partial x} \right)^2 + 2 \left(\frac{\partial U}{\partial x} \right)^2 + 2 \left(\frac{\partial V}{\partial y} \right)^2 \right] - C_2 \frac{\varepsilon^2}{k} \tag{12}$$

where $C_1 = 1.44$; $C_2 = 1.92$; $\sigma_k = 1.0$; $\sigma_\varepsilon = 1.3$.

It should be noted that the computations have ignored any effect which
the magnetic field may have had on the turbulence. Also ignored are any
oscillations of the electrolyte-metal interface.

The five differential equations (6)-(8), (11) and (12) were solved
simultaneously using a computer program developed by Sharma (5). The algorithm
employed was a finite difference procedure with the equations in the form of
"primative variables" (U, V and P rather than stream function and vorticity).
A "staggered" finite difference grid was employed wherein the scalar variables
(P, k and ε) and the velocity components are computed at locations which are
staggered with respect to each other. Grid notes, representing the intersection
of orthogonal (but unequally spaced) grid lines are selected to lie at the
geometric centers of associated small control volumes (see Fig. 2). All scalar
variables are computed at each grid node. The U velocities are computed at
the intersection of the grid lines running in the x direction with the faces
of the control volumes parallel to the y axis. The V velocities are computed
at the intersection of the y direction grid lines with the faces of the control
volumes parallel to the x axis. It should be noted that, in general, the
points at which the velocity components are determined will not lie halfway
between grid nodes.

The differencing procedure was an integrated hybrid difference scheme.
In developing finite difference forms of the differential equations a choice
is to be made between upstream and central differences. The latter is more
precise but entails needless precision and instability at high values of
the ratio of convective to diffusive fluxes (Peclet number). Instead of
employing upstream or central differencing throughout the computation, the

hybrid procedure permits an automatic local selection of upstream or central differencing. The magnitude of the local Peclet number is used as the criterion for the selection.

Boundary conditions on the velocity components were obtained by the "wall function" method described by Launder and Spalding (4). Boundary conditions on k and ε at the walls were supplied implicitly. The method adopted was based upon the presumption that a wall parallel steady boundary-layer regime persists in the immediate vicinity of the wall. Accordingly it was sufficient to account for boundary layer contributions to the balance of k and ε ; and in this way the explicit setting of boundary conditions at the wall surface itself was avoided. Specifically, provision was made to account for the generation of turbulence energy by virtue of wall-dominated shear. The provision was based upon the semi-logarithmic law of the wall (4). The diffusion of k at the wall itself, which requires the value of k at the wall itself, was neglected. For the energy dissipation rate, ε, the near-wall value was fixed from a knowledge of k and the linearity of the turbulence length scale in the vicinity of the wall, thereby eliminating the need to supply the values or flux of ε at the wall boundaries.

Transformation of equations (6)-(8), (11) and (12) into finite difference form is the equivalent of performing a balance on a small control volume such as illustrated in Fig. 2. It is therefore necessary to obtain the transport coefficients at the faces of the control volume, which, in the case of scalar variables, lie midway between grid nodes. It is customary to calculate the transport coefficients at these midway points as the arithemtic mean of the values at adjacent grid nodes. Such a procedure results in erroneous flux computations when the midway point in question lies at an interface between

two regions with vastly different transport coefficients (e.g. a wall). It may be shown (5) that a more appropriate value for the transport coefficient at a midway point is the harmonic mean of the values at adjacent grid nodes and such a mean was incorporated in the computations.

The set of finite difference equations was solved iteratively in a line-by-line fashion by repeated application of the well known tri-diagonal matrix algorithm (TDMA) (6). In this procedure the finite difference forms of equations (6), (7), (11) and (12) are solved, one at a time, along a line of grid nodes. This line is then swept through the mesh in a direction perpendicular to itself. The sweep direction is alternated between the y direction and the x direction as is the sense of the sweep (left to right on one sweep in the x direction, right to left on the next weep in the x direction, etc.). Since, typically, the values of U and V are only weakly dependent on μ_e the equations (11) and (12) were not solved on every iteration but rather every few iterations. Values of U and V obtained on each iteration of (6) and (7) will not necessarily satisfy the equation of continuity (8), consequently the values are adjusted to satisfy (8) on each iteration using a procedure described by Sharma (5). In this way, at convergence, a velocity and pressure distribution is obtained which satisfies all three equations (6)-(8). Under-relaxation is employed during the iterations. The grid used had 11 x 19 nodes, which preliminary calculations indicated was a sufficient number for the required precision.

COMPUTATION OF INTERFACE TOPOGRAPHY

The method by which the shape of the interface between metal and

electrolyte can be calculated is best understood by reference to Fig. 3.
Equations (6) and (7) assume that the interface is a flat one and their
solution yields a pressure distribution for the electrolyte and for the metal.
In reality both liquids have freely deformable surfaces and the computed
pressure distributions are exactly balanced by the hydrostatic pressure
gradients developed as the interfaces deform. Simple force balances therefore
yield the following equation for the height of the interface, h, with respect
to an arbitrary reference position.

$$h = \frac{P_E - P_M}{g\left(\rho_M - \rho_E\right)} \qquad (13)$$

It is noted that this equation assumes that gravitational (rather than
electromagnetic) forces predominate in the downward direction.

CALCULATION OF MASS TRANSPORT RATES AND OF CURRENT EFFICIENCY

The computation of the velocity components, k and ε throughout the molten
electrolyte and metal, described in the previous section, also yields the
distribution of the effective viscosity in the two cell liquids. From this
last distribution it is possible to calculate the distribution of the eddy
(mass) diffusivity throughout the electrolyte by making the usual assumption
that the turbulent Schmidt number is close to unity. The turbulent diffusivity
calculated in this way averaged 27 cm^2/sec over the region of the electrolyte
which is beneath the anodes. This should be compared with a value of 5 cm^2/sec
determined experimentally by Berge et al. (11) for the aluminum layer. From
the eddy diffusivity, the anode-metal distance and the solubility of the
aluminum in the molten cryolite it is then possible to estimate the rate of

mass transport of dissolved aluminum from the metal-electrolyte interface to the anodes where it is reoxidized. Such an estimate yields a rate of mass transport higher than that at which aluminum is being produced in a typical cell.

The explanation for this anomaly is that in the vicinity of the metal-electrolyte interface the turbulent transport of dissolved aluminum (and momentum) is damped by the surface tension at that interface. Consequently, the rate controlling step in the aluminum transport/reoxidation sequence is the transport of aluminum through a concentration boundary layer at the metal-electrolyte interface. Levich (8) has considered mass transport through such surface tension induced boundary layers and derived an equation for the mass flux of dissolved species:

$$j = \left(\frac{D\rho V_t^3}{\sigma_t} \right)^{1/2} C_s \qquad (14)$$

V_t is related to the turbulence kinetic energy by

$$V_t = \sqrt{k} \qquad (15)$$

and consequently equation (14) becomes

$$j = \left(\frac{D\rho C_s^2}{\sigma_t} \right)^{1/2} k^{3/4} \qquad (16)$$

The rate of mass transport from the metal to the anodes was calculated using equation (16). In this calculation the mass transport was assumed to be purely in a vertical direction and to take place only underneath the anodes, i.e. the area available for mass transport was equal to the sum of the

anode cross sections in the cell. The value used for k was obtained by averaging, over the electrolyte, the k distribution obtained in the velocity calculations. C_s was assumed to be the equilibrium value and this value and σ_t were obtained from the literature (7). The current efficiency was then obtained from

$$\text{Current efficiency (\%)} = 100 \left(1 - \frac{\text{Mass transport rate of Al to anodes}}{\text{Al production rate expected from Faraday's law}} \right) \quad (17)$$

RESULTS OF CALCULATIONS AND DISCUSSION

Fig. 4 depicts the isopotential lines in a 185 kiloamp Kaiser Aluminum cell computed by the finite element technique described above, while Fig. 5 shows the computed horizontal components of the magnetic field at the top of the electrolyte pool, together with those measured on the cell using a Hall effect probe. Both these figures are taken from the work of Tarapore (12). In view of the assumptions entailed in the model, the agreement between measured and calculated values appears reasonable.

In Fig. 6 the computed and measured values of metal velocity within the molten metal pool are compared. Metal velocity measurements were determined by measuring the rate of dissolution of iron rods in the aluminum, as described by Johnson (9). The magnitudes of the computed velocities within the metal are comparable with the magnitudes of the measured velocities. However, the computed velocity directions show poor agreement with measured directions in some regions of the cell (e.g. lower left hand edge of each drawing).

Computed velocities in the molten cryolite electrolyte below the level of the bottoms of the anodes are presented in Fig. 7. The computed velocities

are seen to reach higher values than those computed for the molten metal.
Presently there are no data on electrolyte velocities within the Kaiser cell
to enable a comparison of computed and measured velocities. Fig. 8 gives
the values of the turbulence kinetic energy (cm^2/sec) computed for various
points within the molten salt electrolyte. Again there are no experimental
data for comparison with these calculated values.

The calculated value for the current efficiency of the 185 kA Kaiser
cell is 88.5%. It should be noted that the calculated current efficiency is
dependent on physical properties (the solubility of aluminum in cryolite and
the interfacial tension) about which there is some uncertainty (7).

Equation (16) predicts an increase in mass flux (lower current efficiency)
as the electrolyte-metal interfacial tension is lowered. This is consistent
with the results of Belyaev and coworkers and other investigators as reported
by Grotheim (7). These investigators observed that the rate of aluminum
transport at the molten metal-cryolite interface was increased by changes in
metal or cryolite which reduced interfacial tension.

One parameter under control of the cell designer is the arrangement of
the bus-bars in the vicinity of the cell. The mathematical model was used
to predict the relative advantages of quarter risers, end risers and the
novel riser arrangement depicted in Fig. 9 for a cell of a somewhat different
design than the Kaiser 185 kA cell.[*] The riser arrangement appearing in
Fig. 9 is a first attempt at a bus-bar system having greater symmetry than
that of conventional cells. Metal velocities for the three cell designs

---

[*]Since the purpose here is to illustrate the capabilities of the model,
rather than engage in predictions for a particular cell, details of this cell
design are not supplied here but may be obtained from one of the authors (JWE).

appear in Fig. 10 (velocity vectors are drawn with the arrows representing velocities from the tail of the arrow creating a false impression of the aluminum passing through the wall of the cell). The lack of symmetry arises because of a return bus bar positioned 5.7 meters from the left end of the cell; an adjacent potline would have had a similar effect. The relatively small differences between the velocities in the aluminum for the three designs requires explanation. Absolute values of the electromagnetic forces are of no significance, as far as the stirring of the melts are concerned, but rather variations in these forces (in magnitude and direction). In the aluminum pool the currents "fringe", i.e. there is a tendency for the current to flow outward through the cell walls, as well as vertically downward. The predominant stirring forces in the aluminum are therefore caused by variations in forces arising from currents internal to the cell. Since the three designs have identical internal current distributions, there is little variation in the stirring of the aluminum.

In contrast, within the molten electrolyte there is little fringing of current and the stirring effects due to internal currents are less significant. This can be seen in Fig. 11 where melt velocities in the cryolite are plotted and the different riser arrangements are seen to yield quite different velocity distributions. The end riser cell displays a complex circulation pattern with high velocities in the cell corners.

Interface contours for the three riser arrangements appear in Fig. 12 where the novel riser design is seen to result in more bowing of the interface than the end riser design while the quarter riser design shows the least bowing of the three designs. It should be noted that the interface topography

is affected by the absolute values of the electromagnetic forces.

The current efficiencies for the three riser designs are reported on in the first column of Table I. It appears that the complex circulation pattern of the end riser cell, with its high velocity gradients, results in more turbulence in the electrolyte, a greater transport of aluminum and lower current efficiency, than the quarter riser or novel riser design. The novel riser design does not yield a current efficiency significantly different from that of the quarter riser cell.

The anode bus and anode rods make a substantial contribution to the magnetic field within the cell. In contrast to the cathode ("ring") bus, these external conductors are not shielded by the steel shell of the cell. It might be conjectured that the cell performance would be improved by shielding the anode bus. This could be achieved in practice by replacing the aluminum cell covers typically used, by steel ones. The results of such shielding are presented in the second column of Table I. The model predicts that such shielding would be effective in the case of end riser cells but would reduce the current efficiency of a quarter riser cell. Again it is stressed that absolute values of stirring force are not significant as far as velocities and current efficiencies are concerned, but rather their variation. Thus, while screening the anode bus reduces the total magnetic field in all cases, in the case of the quarter riser cell it simultaneously enhances its variation. Screening both the anode bus and the anode rods would be much more difficult to achieve in practice; the results of such screening appear in the third column of Table I. The model predicts that this screening would be beneficial for all three cell designs.

CONCLUDING REMARKS

The mathematical model presented here should be regarded as a preliminary one; simplifying assumptions have been made and the physical properties used in the computations have, at present, uncertain values. As a consequence, it would be inappropriate to attach quantitative significance to some of the results (e.g. current efficiencies) reported here. However, more credibility can be attached to relative predictions of the model, for example that the performance of end riser cells may be inferior to that of a quarter riser cell. It should also be recognized that the model does not involve any adjustable parameters.

It is suggested that at this stage the model is a semi-quantitative tool that may be useful in the design and development of Hall cells. The model is capable of improvement, for example by the incorporation of the effect of gas stirring, but the present model is an appropriate departure point for future improved models.

ACKNOWLEDGEMENTS

LIST OF SYMBOLS

C_1, C_2	constants in the k-ε turbulence model
D	diffusivity of solute
C_S	concentration of solute at interface
E	electric potential
F	electromagnetic force vector
h	height of electrolyte-metal interface with respect to reference position
H	magnetic field vector
J	current density vector
j	mass flux of solute at interface
k	turbulence kinetic energy
P, P_E, P_M	pressure, pressure in electrolyte, in metal, with respect to reference position
$\hat{r}, \hat{r}'$	vectors indicating position in melt
U	x direction time averaged velocity component
V	y direction time averaged velocity component
V_t	fluctuating part of turbulent velocity
x	long horizontal direction in cell
y	short horizontal direction in cell
ε	turbulence kinetic energy dissipation rate
μ	magnetic permeability
μ_1, μ_t, μ_e	laminar, turbulent and effective viscosity
ρ, ρ_E, ρ_M	density, of electrolyte, of metal
σ	electric conductivity

σ_k, σ_e turbulent Prandtl number for k, ϵ

σ_t interfacial tension

REFERENCES

(1)   R. F. Robl, W. E. Haupin and D. Sharma, paper no. A77-35 presented at the AIME annual meeting, Atlanta, Georgia, 1977, available from the Metallurgical Society of AIME, New York, N.Y.

(2)   JANAF Thermochemical Tables, 2nd ed., U.S. Dept. of Commerce, Nat. Bureau of Standards, Washington, 1971.

(3)   R. F- Robl, "Influence by Steel Shell on Magnetic Fields within Hall-Heroult Cells" in "Light Metals 1978, Vol. 1", pp. 1-14, The Metallurgical Society of AIME, New York, N.Y., 1978.

(4)   B. E. Launder and D. B. Spalding, Computer Methods in Applied Mechanics and Engineering, vol. 3, 269-289 (1974).

(5)   D. Sharma, "Details of an Efficient Computational Procedure for the Prediction of Convective Heat, Mass and Momentum Transfers," Report ATG/TN/DN/41, Advanced Technology Group, Dames and Moore, Denver, Colorado.

(6)   Dale U. vonRosenberg, "Methods for the Numerical Solution of Partial Differential Equation," Elsevier, New York, N.Y., 1969.

(7)   K. Grjotheim et al., "Aluminum Electrolysis, The Chemistry of the Hall-Heroult Process," Aluminum-Verlag GmbH, Dusseldorf, 1977.

(8)   V. G. Levich, "Physicochemical Hydrodynamics," pp. 690-698, Prentice-Hall, Inc., Englewood Cliffs, N.J., 1962.

(9)   A. F. Johnson, "Metal Pad Velocity Measurements in Aluminum Reduction Cells" in "Light Metals 1978, Vol. 1," pp. 45-58, The Metallurgical Society of AIME, New York, N.Y., 1978.

(10) K. Grjotheim et al., Metallurgical Transactions, Vol. 2, 199-204 (1971).

(11) B. Berge et al., Metallurgical Transactions, Vol. 4, 1945-1952 (1973).

(12) E. D. Tarapore, "Magnetic Fields in Aluminum Reduction Cells and Their Influence on Metal Pad Circulation" in "Light Metals 79", vol. 1, pp. 541-550, The Metallurgical Society of AIME, New York, N. Y. (1979).
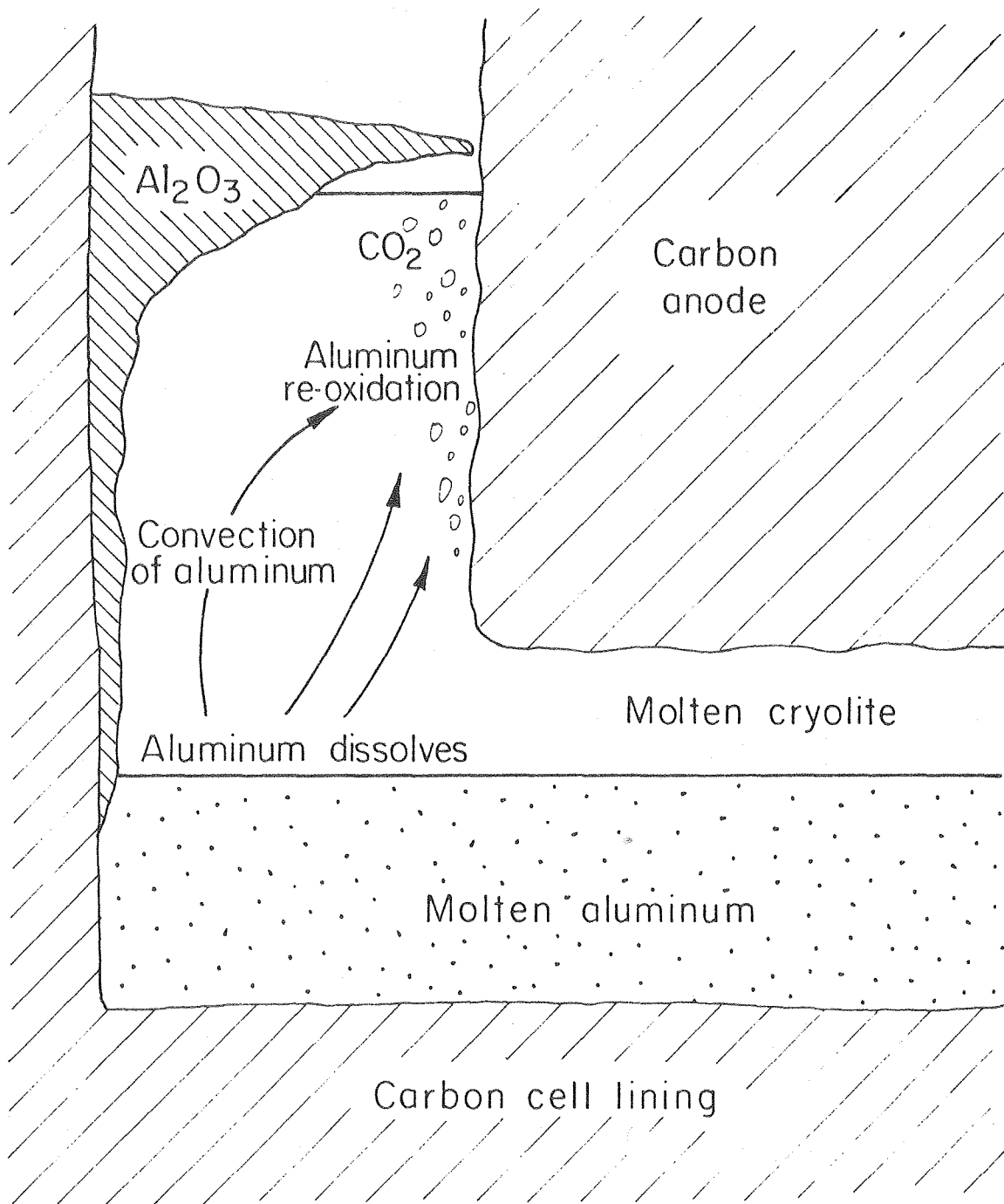
TABLE I

Computed current efficiencies for various cell modifications

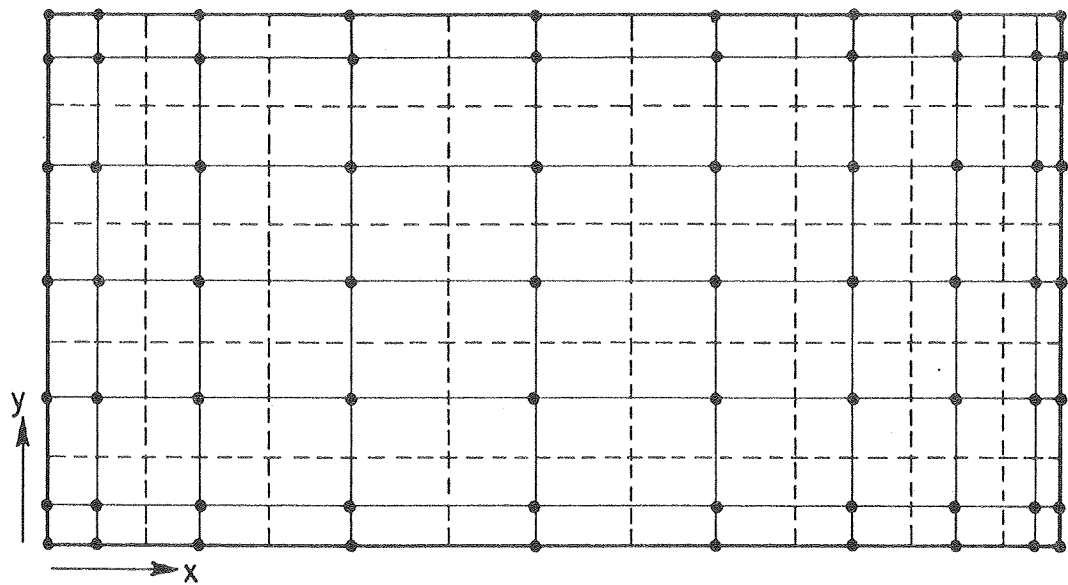|	Unshielded anode bus and rods	Shielded bus, unshielded rods	Shielded bus, shielded rods
Quarter riser	93.8	92.9	94.9
End riser	88.6	90.3	92.7
Novel riser	93.4	93.4	95.5

Figure Captions

Fig. 1   Transport and re-oxidation of part of the aluminum product in Hall-
Héroult cells. XBL784-8016

Fig. 2   Finite difference grid employed in the melt flow calculations.
XBL793-5868

Fig. 3   Figure illustrating the method of calculating interface position,
based on the balance between pressure and hydrostatic forces.
XBL809-5927

Fig. 4   Isopotential lines (volts) in a 185 kA Kaiser cell computed by the
finite element technique. XBL7811-6172

Fig. 5   Computed and measured components of the horizontal magnetic field
components (gauss) within the electrolyte of the 185 kA cell.
XBL7811-6173

Fig. 6   Calculated and measured velocities within the molten aluminum of
the 185 kA cell. XBL7811-6175

Fig. 7   Computed velocities within the electrolyte of the 185 kA cell.
XBL7811-6176

Fig. 8   Computed values of the turbulence kinetic energy within the
electrolyte of the 185 kA cell. XBL7811-6177

Fig. 9   A bus bar arrangement ("novel" risers) designed to provide a more
symmetrical arrangment of conductors around each cell. XBL809-5928

Fig. 10   Computed metal velocities for three cells differing only in the
design of their risers. XBL809-11702

Fig. 11   Computed electrolyte velocities for three cells of different riser
design. XBL809-11704

Fig. 12 Computed interface topography for the three cells of differing riser design. XBL809-11703

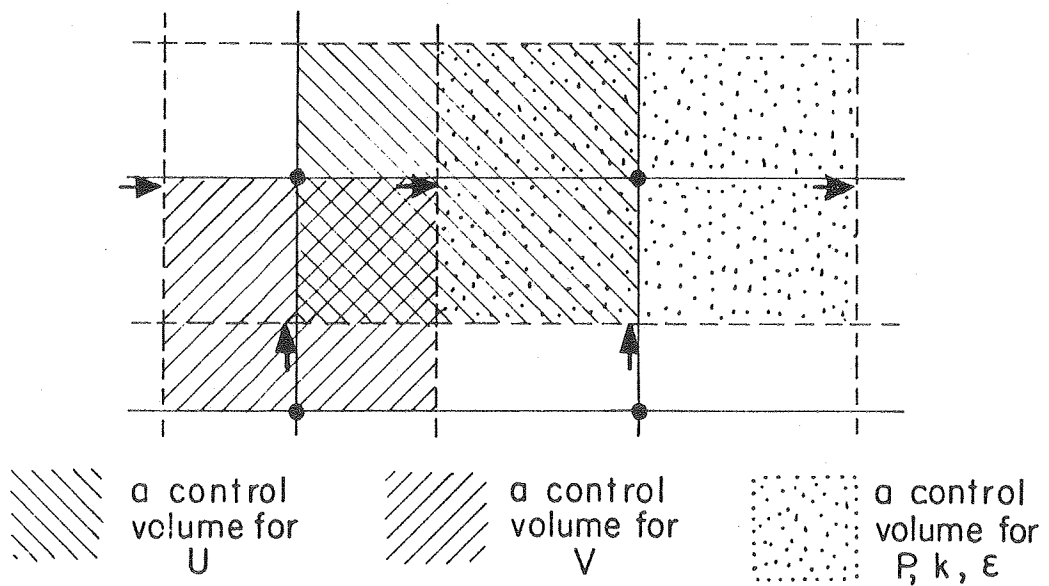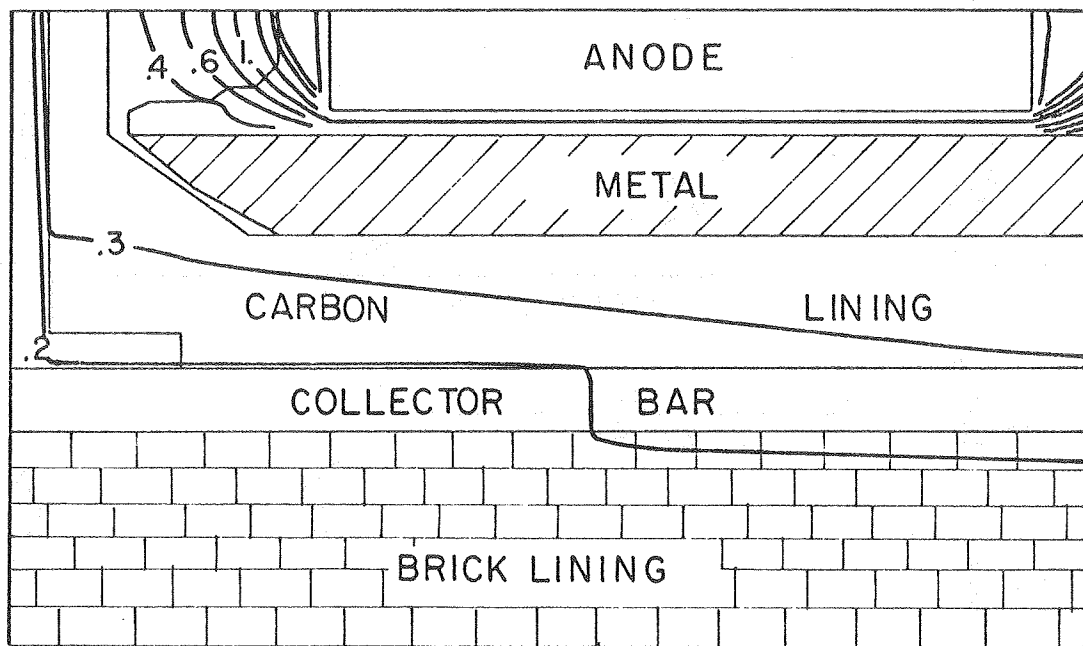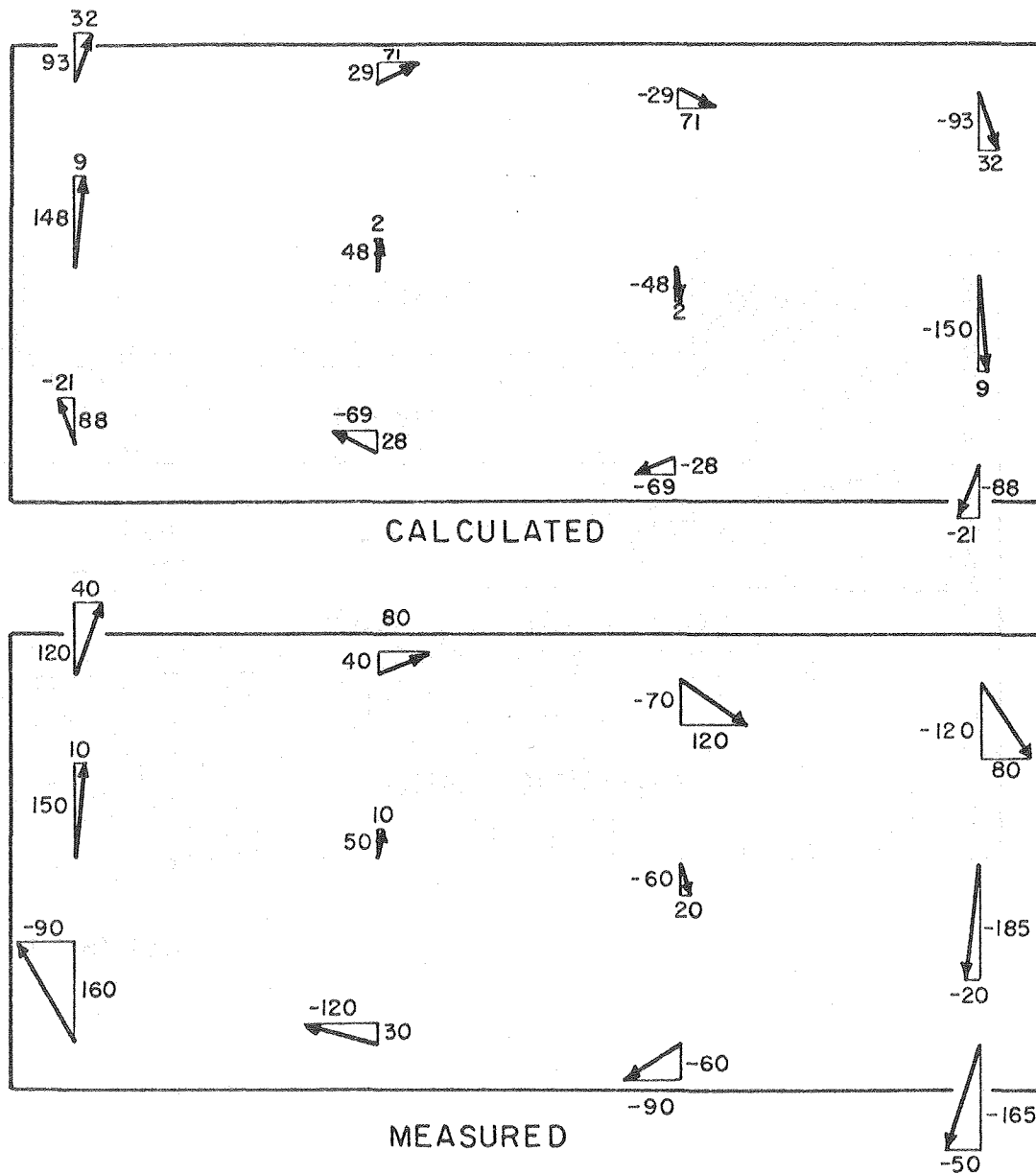Fig. 1   Transport and re-oxidation of part of the aluminum product in Hall-
Héroult cells.

Fig. 2 Finite difference grid employed in the melt flow calculations.
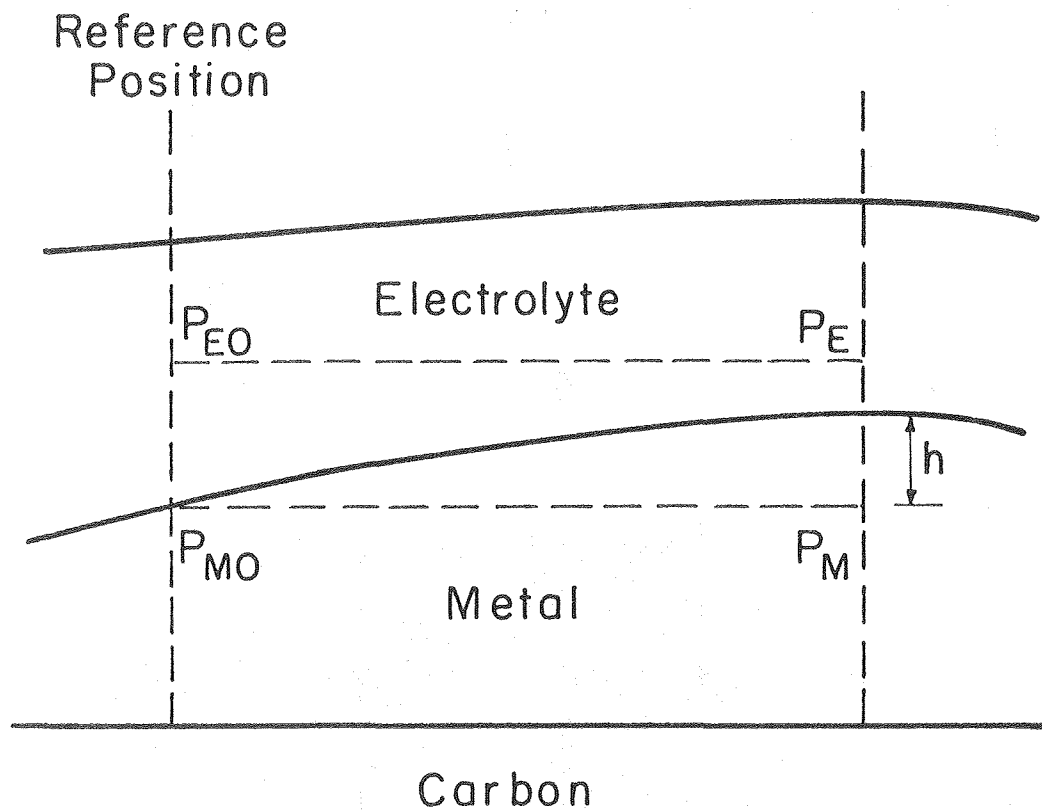
Fig. 3. Figure illustrating the method of calculating interface position, based on the balance between pressure and hydrostatic forces.
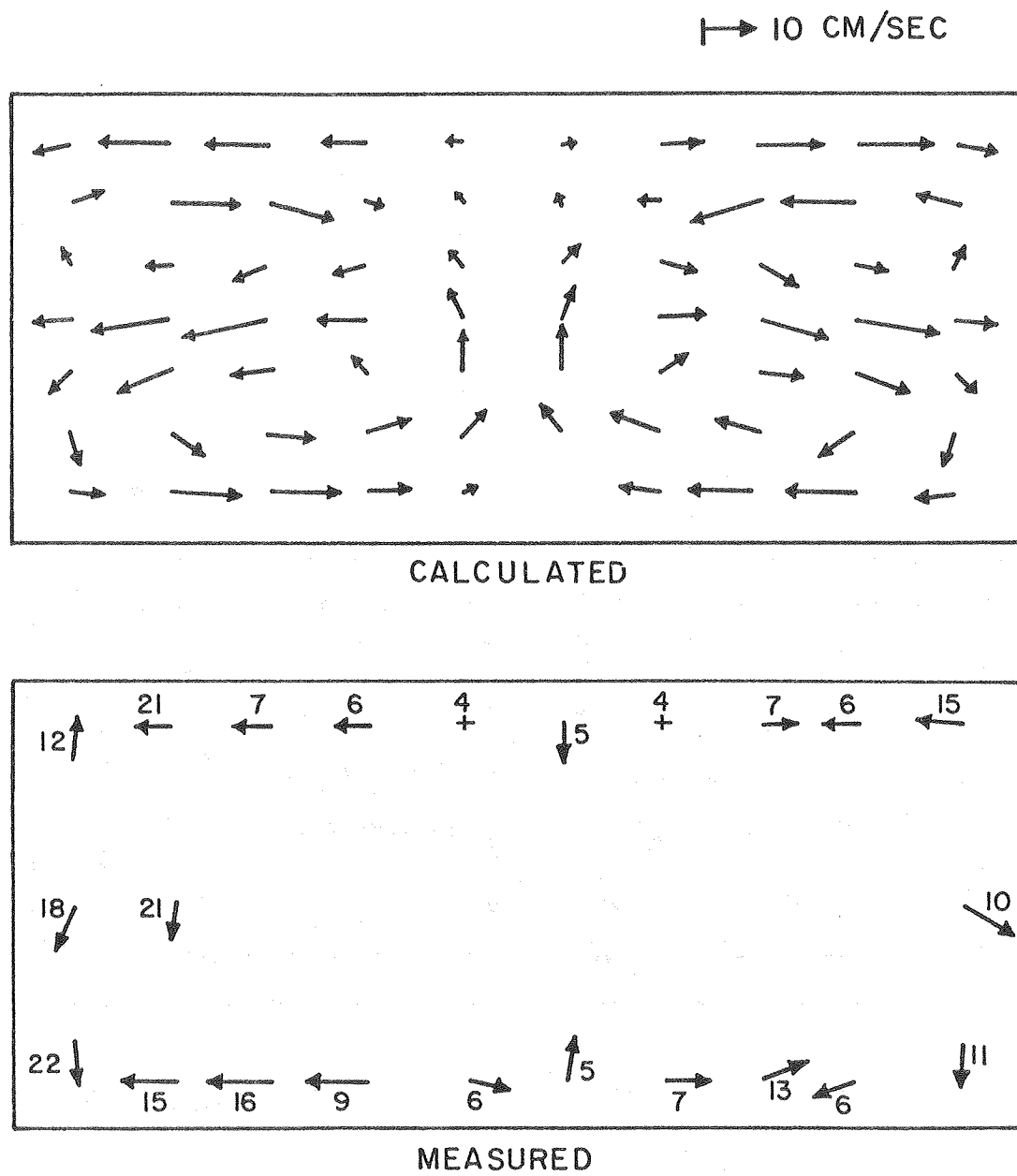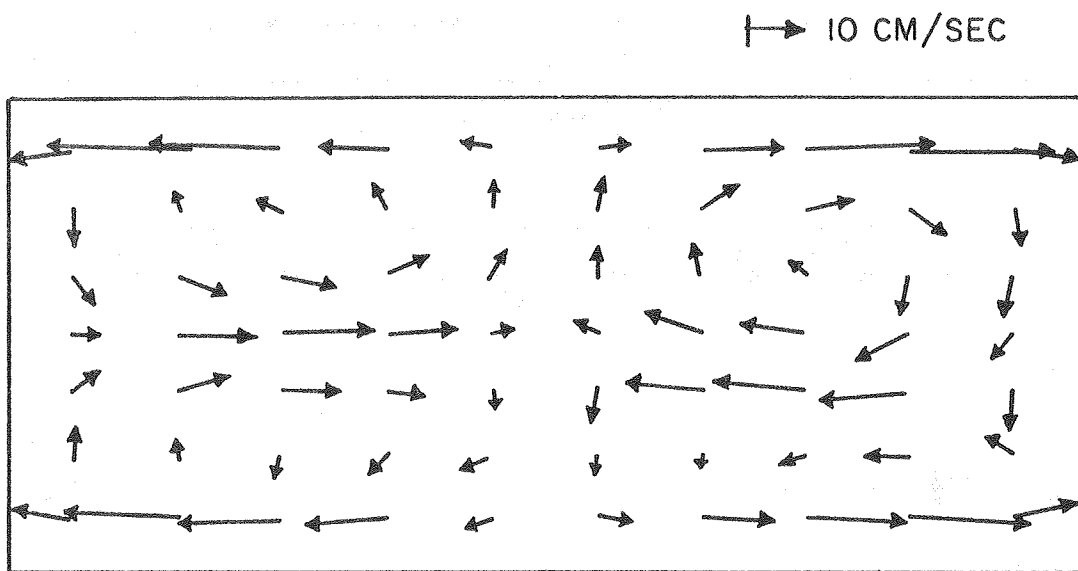
XBL7811-6172

Fig. 4 Isopotential lines (volts) in a 185 kA Kaiser cell computed by the
finite element technique.

Fig. 5 Computed and measured components of the horizontal magnetic field
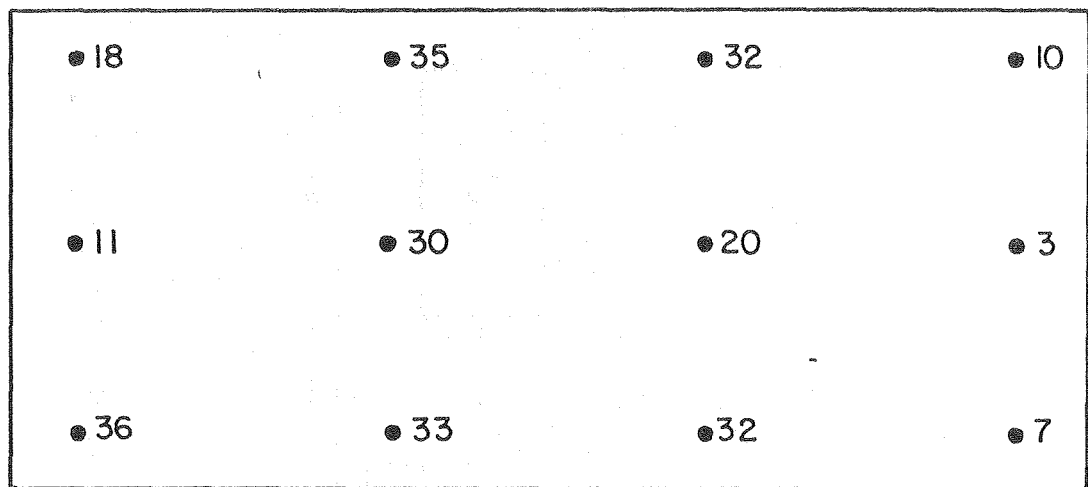components (gauss) within the electrolyte of the 185 kA cell.

⊢→ 10 CM/SEC

CALCULATED

MEASURED

XBL 7811-6175

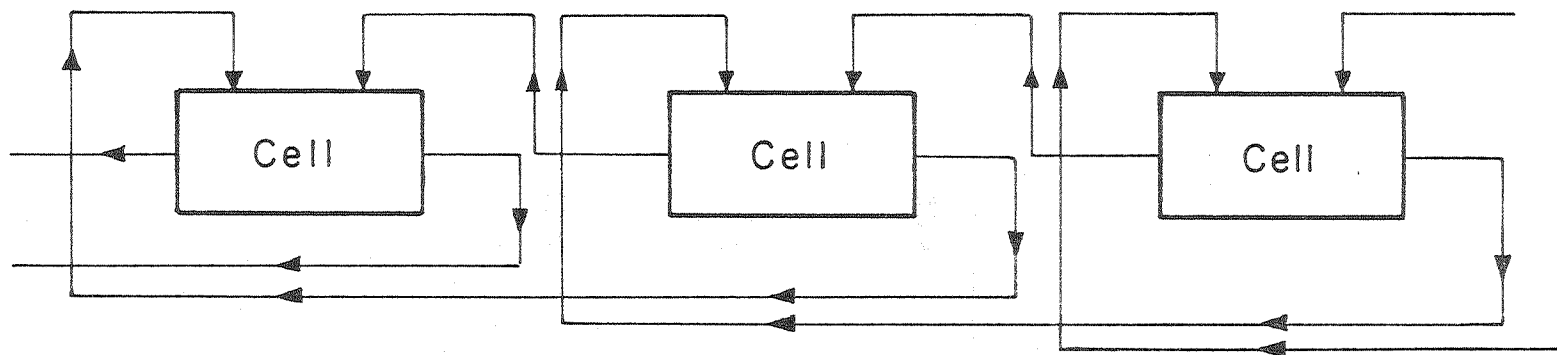Fig. 6 Calculated and measured velocities within the molten aluminum of
the 185 kA cell.

Fig. 7 Computed velocities within the electrolyte of the 185 kA cell.
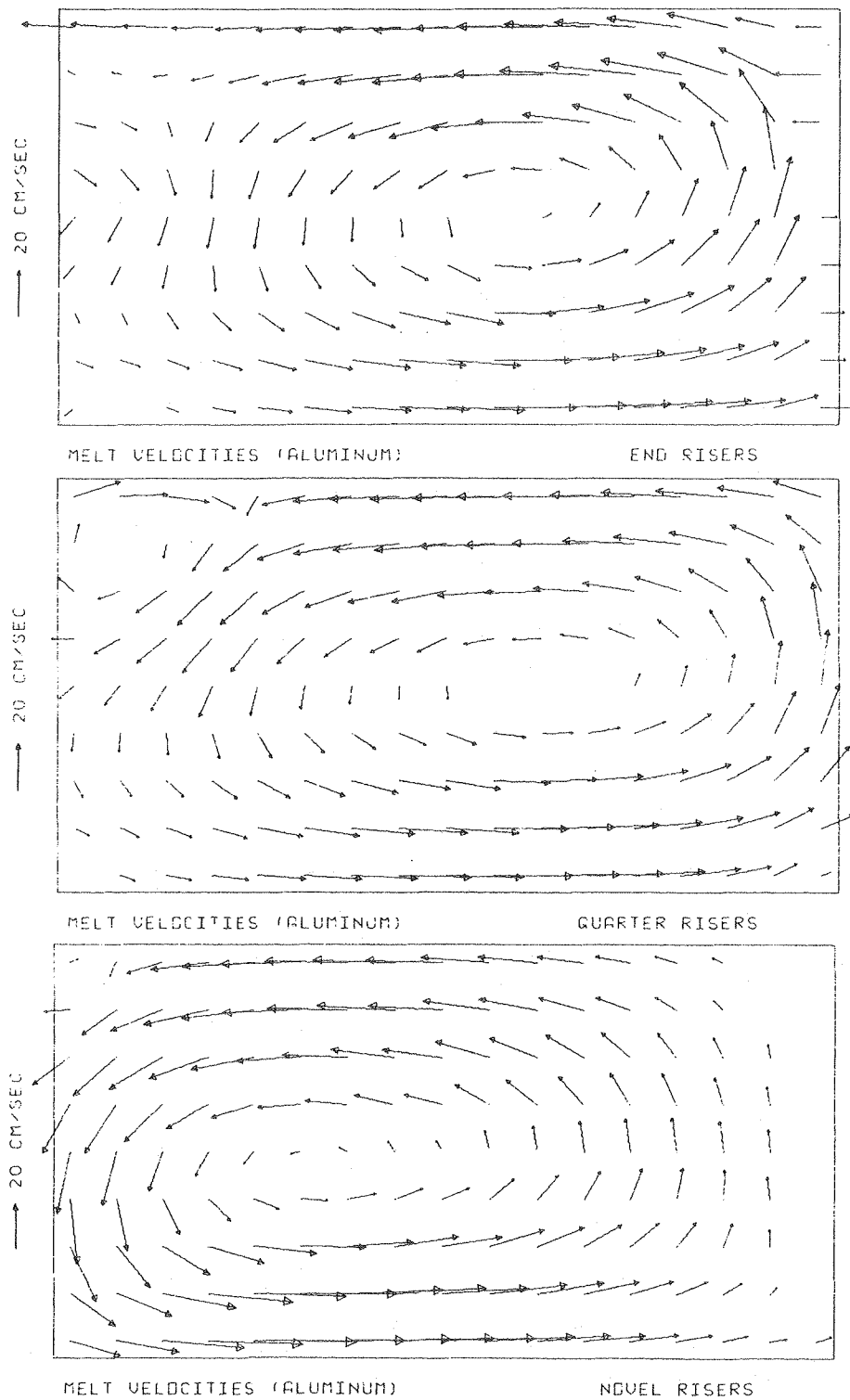
XBL 78ll-6l77

Fig. 8 Computed values of the turbulence kinetic energy within the
electrolyte of the 185 kA cell.

XBL 809-5928

Fig. 9   A bus bar arrangement ("novel" risers) designed to provide a more symmetrical arrangement of conductors around each cell.
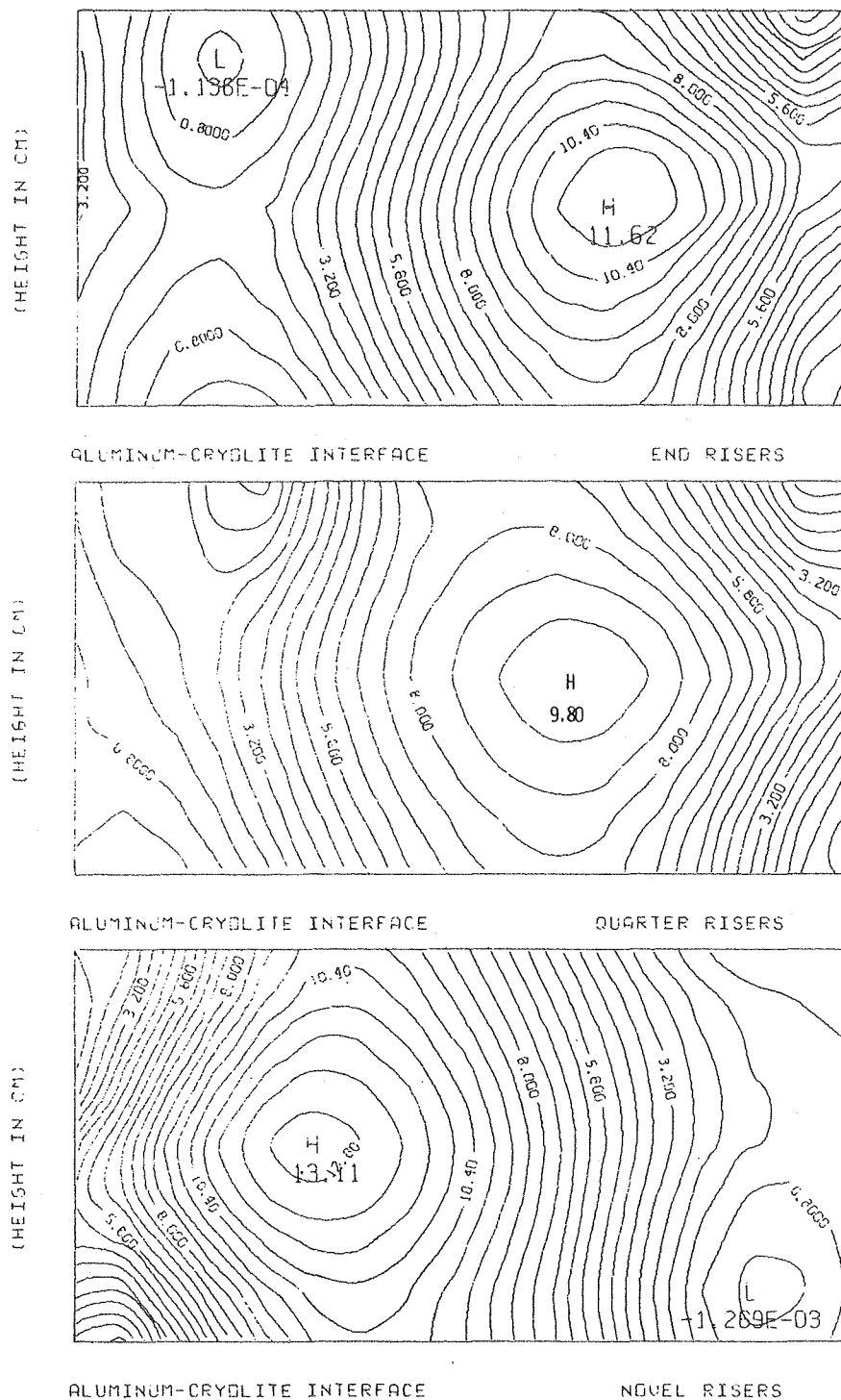
MELT VELOCITIES (ALUMINUM)   END RISERS

MELT VELOCITIES (ALUMINUM)   QUARTER RISERS

MELT VELOCITIES (ALUMINUM)   NOVEL RISERS

XBL 809-11702

Fig. 10 Computed metal velocities for three cells differing only in the
design of their risers.
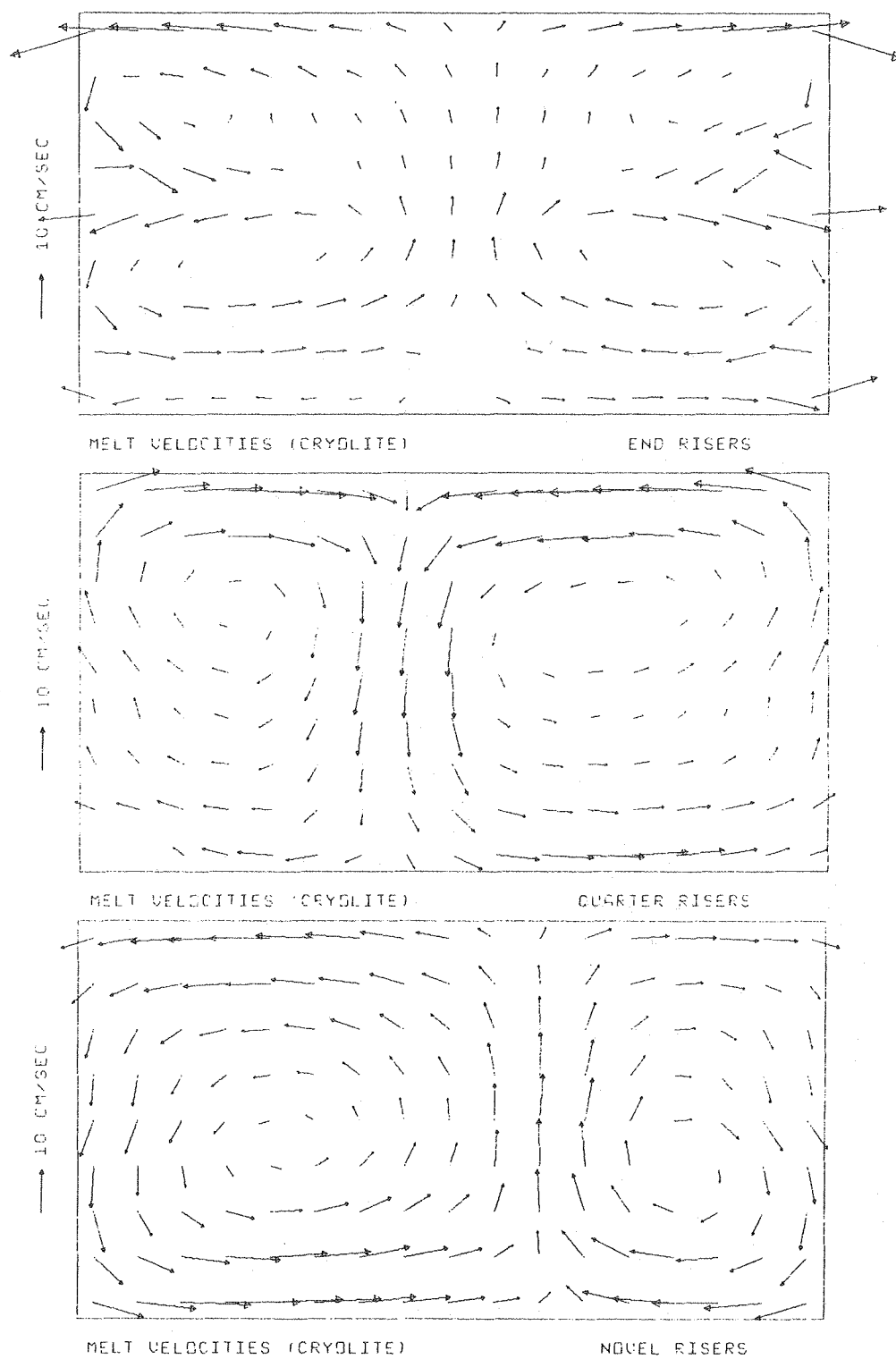
Fig. 11 Computed electrolyte velocities for three cells of different riser design.

XBL 809-11703

Fig. 12   Computed interface topography for the three cells of differing
riser design.